Title

Co-Registered 3D Laser Speckle Endoscope

Permalink

https://escholarship.org/uc/item/4db0g8dk

Author

Jabbari, Alexander

Publication Date

2016

UNIVERSITY OF CALIFORNIA,
IRVINE

Co-Registered 3D Laser Speckle Endoscope

THESIS

submitted in partial satisfaction of the requirements
for the degree of

MASTER OF SCIENCE

In Biomedical Engineering

by

Alexander Jabbari

Dissertation Committee:
Professor Bruce Tromberg, Chair
Associate Professor Bernard Choi
Associate Professor Anthony Durkin

2016

DEDICATION

To

my parents, family, and friends

for all the unwavering support and encouragement

To always try your best

TABLE OF CONTENTS

LIST OF FIGURES

LIST OF TABLES

ACKNOWLEDGMENTS

First and foremost I would like to thank my committee chair Bruce Tromberg. You have pushed me to do better every year and always had complete faith in my ability to achieve whatever goal you set out for me. Your never ending optimism, while frustrating at times, seems now to be something that was invaluable throughout this experience. Secondly, I would like to thank my two other committee members, Anthony Durkin and Bernard Choi. Both of you have been supportive of me for many years, even before attending graduate school. Bernard's straightforwardness and honesty was a necessity in completing this degree. Without Tony Durkin's grounded advice and willingness to provide any assistance he could offer this project would never have been completed.

I would like to thank the many people who helped me throughout this project, from setting up equipment, taking and analyzing data, lending an ear to theories or ideas, or general helpfulness. You all share in this accomplishment and I thank you; Christian Crouzet, Sean White, Alex Matlock, Tom O'Sullivan, and the rest of the DOSI lab at the Beckman Laser Institute. Financial support was given by the University of California, Irvine, and the NIH Grant (P41EB015890).

Lastly, I would like to thank two people who encouraged the notion of graduate school on me; Dr. Robert Brown and Dr. Alessandra Forcucci. If it wasn't for Robert's initial gamble to work with me and both of them advising that I do something meaningful with my life, I would not be here. I owe so much of this accomplishment to the two of you.

ABSTRACT OF THE THESIS

Co-Registered 3D Laser Speckle Endoscope

By

Alexander Jabbari

Master of Science in Biomedical Engineering

University of California, Irvine, 2016

Professor Bruce Tromberg Irvine, Chair

The problem addressed in this thesis is the need for incorporating multiple functionalities into one minimally invasive surgical probe. A novel endoscope probe was designed with two 1mm cube cameras and an optical fiber inside a 3D printed casing, 7mm in diameter. This probe combined stereoscopic imaging, in order to obtain quantitative 3D measurements, and laser speckle contrast imaging, for quantitative flow analysis. 3D surface mapping was validated by comparing computed coordinates against their known real-world values. Laser speckle contrast imaging was validated through an *in-vivo* and *ex-vivo* study comparing the new micro-camera to an existing lab-grade sensor. Both sub-systems yielded results that indicate accuracy and sensitivity equivalent to existing devices. The combination of the two functionalities allows for highly accurate spatially resolved 3D surfaces. These surfaces are combined with a co-registered laser speckle contrast image for later analysis. Presented are the results from all validation studies and finalized dual functionality probe.

INTRODUCTION

Medical imaging has become one of the most prevalent methods of preventing and diagnosing diseases in the body. The most common imaging modalities used in current medical practices include Magnetic Resonance Imaging (MRI), X-Rays, Positron Emission Tomography (PET), and computed Tomography (CT). These methods utilize powerful techniques to achieve high-resolution structural and functional images of the human body that aid in locating and diagnosing a myriad of medical conditions. Despite their utility, some of these imaging modalities use ionizing radiation, radioactive isotopes, or other techniques that can be harmful or too invasive to allow for frequent use on an individual patient. This limitation in repeat imaging on a patient with long-term medical conditions can cause doctors to miss critical changes in their patient's health[1]. Due to the nature of the aforementioned imaging techniques, other methods have been investigated and implemented over the past several decades that minimize the invasiveness of the imaging procedure and remove the harmful side effects present in the common existing modalities.

One such imaging technique is diffusive optical imaging. This technique uses near-infrared spectroscopy (NIRS) to provide quantitative information on the concentrations of specific molecules in tissue[2]. By using low power lasers and detecting signals from tissue either in transmission or reflection geometries, clinical diagnoses can be made without causing a patient to ingest potentially harmful chemicals or be subject to ionizing radiation. Recently, several advancements, such as optimal wavelength selection and optimal source detector separation have been made to increase the accuracy and speed of the current diffuse optical imaging methods (DOI)[3,4]. These advances in technology have allowed clinicians to track and observe changes that might have been previously overlooked in the past using these new imaging techniques. For example some of these longitudinal studies are used in cases of tracking breast cancer tumors or cerebral activation[5,6]. At the same time, reductions in size of the core components for these modalities have enabled smaller, less costly devices that limit the invasiveness of many internal procedures[7].

Laser Speckle Contrast Imaging (LSCI) is one such diffuse optical imaging technique that has undergone significant recent technological advances. LSCI is a wide-field imaging technique that provides structural information and blood flow analysis of superficial vasculature in living tissue[8]. This emerging method utilizes the scattering of coherent light to analyze the interference patterns created when light reaches each pixel at slightly different times due to the difference in travel distance. These images, referred to as speckle patterns, can be evaluated to give information pertaining to the motion of the scattered particles. Lately, LSCI's predominant use has been in neurovascular imaging applications in animals and humans. Although these applications have required invasive procedures to access the subject's vasculature for imaging purposes, the foundation exists for examining blood flow in small localized regions. Generally, a small region of interest (ROI) of the vasculature is sampled to gain information regarding the tissue's overall blood flow. This prior work has shown compelling results in analyzing blood flow[9] so far as it has enabled . However, these applications have also drawn attention to the limited penetration depth of the technology, which typically is about 1mm, depending on optical properties of the tissue[10]. While this prevents LSCI from achieving full-body scans and deep tissue images like MRI, this limitation can be circumvented through the miniaturization of current technology and delivered endoscopically for minimally invasive procedures.

One of the main minimally invasive surgical (MIS) devices used around the world is the endoscope. Over the years endoscopes have evolved from rigid tubes inserted through the mouth to flexible fiber bundles capable of acquiring videos images of different internal regions of the body. Endoscopes were previously only capable of enabling visualization of gastrointestinal tracks, stomach, or nasal cavities, but the miniaturization of technology has allowed for drastic improvements in endoscope functionality, incorporating both visualization and tissue manipulation. Working channels that held tools for performing biopsies on lesions and polyps became a standard medical practice. Eventually additional functional tools, including advance surgical tools were included to surpass diagnostic usages and move toward treatment purposes. But even between treatment and diagnosis, endoscopes generally are limited in their ability to yield more than just two-dimensional visual information. There is a compelling need in endoscopic procedures for surgeons to have interactive three-dimensional quantitative measurements. Today, optical endoscopy is a standard tool in hospitals but is limited due its access to only two-dimensional imaging, despite fact that common pathologic structures such as…… have three-dimensional structure this is likely relevant to diagnosis. Generally endoscopic procedures focus on imaging the colon, intestines, and stomach. Surgeons usually look for small abnormalities that differ from surrounding tissue in order to make diagnosis. They estimate the size and severity based on the images shown to them and their own skill and experience. Exact measurements (and access to three-dimensional information) can only be made either through exploratory surgery or a biopsy.

Stereoscopic imaging is a method to achieve a three-dimensional image by presenting two offset images to the right and left eye[11]. Depending on either active or passive methods, a 3D scene can be formed from these two vantage points. A passive stereoscopic image pair uses two superimposed images where depth is displayed with the use of polarizing filters[12]. This method usually requires a unique type of glasses needed to observe the apparent depth. Active stereoscopic imaging is achieved by alternating the right and left images at sufficiently high frequency to give the appearance that the two images have fused together into one composite 3D scene[10]. Yet almost all passive and active methods provide an end result that has the appearance of three-dimensions, but without any dimensional values.

Technological advances in computer vision have allowed for quantitative information to be gained from stereo images in a fast and reliable manner. Epiploar geometry, the geometric relations between a 3D scene and 2D images, is implemented to extract real-space coordinates from a stereo image pair[9]. Here, knowing simple camera relations and properties, it is possible to recreate full 3D scenes from two images. When these 3D scenes are constructed from a pair of stereo images and real world coordinates are calculated, it is referred to as triangulation. Triangulation computes coordinates in real space, found in two images, relative to one of the cameras using the cameras intrinsic and extrinsic properties.

The primary focus of the work presented in this thesis was to combine both 3D stereo triangulation and LSCI into an endoscopic probe head. Pairing 3D stereo triangulation and LSCI into one device provides the possibility to overcome two major limitations. By creating a system that can accurately give 3D dimensionality and analyze flow dynamics during MIS allows for greater information to be gained while not being constrained by skill or experience of the surgeon. Furthermore, including a method for evaluating blood flow inside the body grants the additional information not normally achieved through common DOI. Combining these two modalities can greatly increase the effectiveness of endoscopic procedures by way of tracking areas of interest at more frequent intervals than established methods.

This thesis describes the validation of two different imaging modalities needed to create a prototype which can effectively yield accurate three-dimensional measurements as well as blood flow analytics. In Chapter, a validation study is performed to characterize the accuracy of a stereoscopic imaging system using a newly develop sensor, the NanEye. Chapter 2 discusses two different LSCI studies aimed at establishing the sensitivity of the NanEye. Chapter 3 displays the full functionally of the probe after both imaging techniques have been incorporated into one endoscopic probe head. Finally, Chapter 4 concludes the results and the importance of this advancement while discussing the limitations and additional future work needed.

Chapter 1: Stereoscopic 3D Imaging

Over the last 50 years multiple methods for discovering 3 dimensional (3D) information of an image or scene have been described in the literature; laser triangulation, time of flight, phase structured fringe pattern light, and stereo vision to name a few [13]. These methods can generally be classified as either active or passive. Active methods require a controlled modulation of the intensity from the light source to obtain the 3D data points. Oppositely, passive methods rely on ambient or stable light. Active and passive techniques have tradeoffs between speed, accuracy, and computational power required. Stereo vision is one of the fastest and least computationally demanding methods of those that have been described, but it requires several steps that impose their own limitations. Detecting matched points in a pair of stereo images and a form of triangulation are the two most important steps in order to gain quantitative 3D data using stereo vision. There are dozens of different feature detection algorithms, each one different depending on the type of element being searched for[14]. Scale-Invariant Feature Transform (SIFT) and Speeded Up Robust Features (SURF) are two robust matching algorithms used to correctly identify localized features between images[15,16]. Matched features between two images can then be triangulated to create individual 3D points or an entire scene. One of the primary focal points of this work was the use of stereo vision with micro-scale cameras to generate 3D surfaces comparable with current 3D endoscopic devices.

Normally minimally invasive endoscopic procedures provide a monocular view. But over the years significant work has been made to achieve 3D endoscopic viewing. Early attempts at attaining 3D images used a dual lens system with complementary multibandpass filters to create stereo image pairs and view the overlapping images[17]. Systems such as this one require an intricate apparatus just to acquire the data needed to create 3D images. Still, results from this method only yield a 3D view of the scene and quantitative analysis cannot be performed. Even combining other well known medical imaging conventions such as optical coherence tomography (OCT) and implementing an optical frequency domain imaging (OFDI) system requires a complex series of optical components and remain computationally demanding[18]. Other improvements in MIS and 3D imaging were to use structured light to generate spatially high resolution 3D images. The use of structured light did result in quantitative measurements and a resolution of 100μm when resolving 3D features[19]. This results in one of the most accurate 3D systems but does come at the cost of high computational power and sensitivity to movement fluctuations. All of the aforementioned work shows significant improvements in the combination of MIS and 3D imaging but either requires numerous components or a high level of computational power. The device that I describe is not limited but these constraints.

1.1 Stereo Vision

Similar to the way human eyes process and understand three dimensional scenes, stereo vision uses two cameras to obtain offset images of the same scene. Just as in human eyes, the two images are displayed as a right and a left side. The disparity between these images can be analyzed to obtain quantifiable measurements and relative depth from the scene imaged[20].

Over time this technique has been used in a multitude of applications in both the electronic world as well as in the biomedical world[21,22,23]. The principles of using two offset images to display 3D scenes was the basis of 3D displays on devices ranging from movies and display monitors for gaming devices[24]. NVIDIA has implemented a stereo vision component to many of their graphics cards. This display alternates a right and left image between 60 and 120 Hz to give the give the appearance of depth on screen. Usually though, these displays need some form of polarized glasses in order to achieve the desired results. In 2011 Nintendo released a handheld game console, Nintendo 3DS that implemented an autostereoscopic display. This device had the ability to display 3D images or videos without the use of glasses or other accessories. In the case of the Nintendo 3DS, this was one of the first commercially available handheld 3D display device. As sensors continued to reduce in size, and computing speed increased; applications of stereo vision began to enter the medical device world. Today there are several 3D endoscopes based on stereo vision[25]. The results from these devices range from displaying a surface map with little dimensional information all the way to full 3D scene reconstructions with accurate dimensional information.

Compared to other 3D imaging methods, stereo vision can be executed at variable speeds with minimal data acquisition time. Compared to time of flight or structure from motion, stereo vision requires a minimum of two vantage points from the scene. Since this can be accomplished with two cameras working simultaneously, stereo vision does not require large storage space. The downside of this method is without a point matching and triangulation algorithm, the displayed 3D scene only gives the appearance of depth and rarely can dimensional analysis be performed.

For the purposes of this work, two AWAIBA NanEye 2D CMOS sensors (Awaiba GmbH) were placed in parallel with one another at a separation of 4.0 millimeters. The NanEye has a resolution of 250 pixels (W) by 250 pixels (L) and takes single images or video ranging from 43 to 60 frames per second (fps). Normally, for stereo vision to be effective the two images must to be co-registered or rectified with one another. This ensures that both images lie on the same plane and is important for triangulation of points later on. To circumvent the need for rectification the cameras were placed on the same axial plane as each other. Due to the NanEye's large field of view (FOV), 120 degrees, a 4.0 millimeter separation was sufficient to maintain significant overlap in the two images, thereby maximizing the number of possible feature matches between images. Figure 1.1 shows an example of a stereo image pair taken with the two NanEye cameras. The target object is a spherical object with a diameter of 40mm. It was placed inside a 3D printed cylinder, radius of 50mm. No illumination was used to capture the images in Figure 1.1, and the object was placed at the maximum length of the camera's working distance, 35mm. With no illumination and at the edge of the devices working distance, the images appear blurry, yet they do provide enough distinct features for image matching to be performed on them.

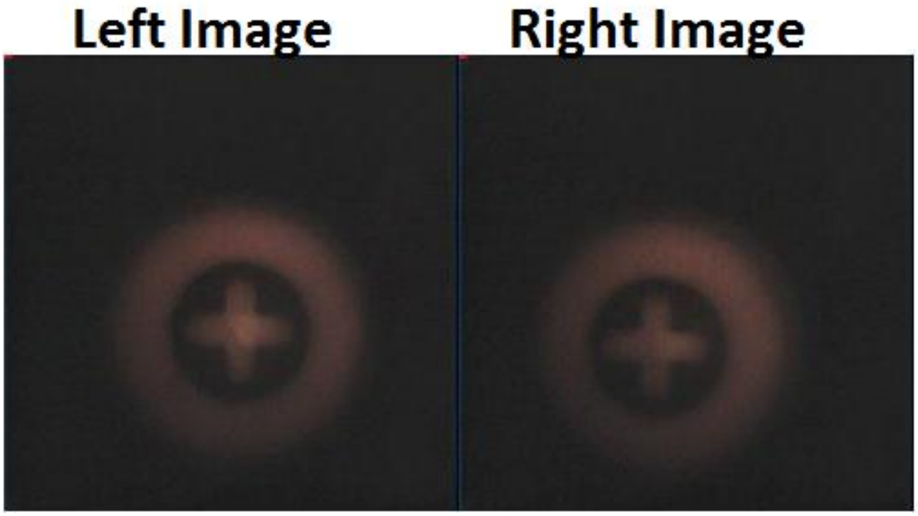

Figure 1.1: Stereo Image Pair. Two images offset by 4.0mm.

1.2 Feature Matching

Feature detection or feature matching is the concept of computing abstractions from image information, usually in localized areas, and correctly identifying the same information in a different image[26]. Usually the identifiers matched between images are, edges, corners, or ridges of some object. Over the years many detection algorithms have been developed, such as Canny, Sobel, FAST, or MSER to name a few. However, these are simply feature detection and not true matching algorithms. Scale-Invariant Feature Transform (SIFT) and Speeded Up Robust Features (SURF), are two well known algorithms that not only detect features in two corresponding images but also match the features between two images.

SIFT creates a database of feature descriptors in a training image. This database is used to identify the same features inside a test image, even if the test image is populated with significantly more objects. A key part that distinguishes SIFT from other feature recognition algorithms is that descriptors should be recognizable under changes to the image such as, scaling, noise, illumination, and even translations. There are four main stages for determining and matching features using the SIFT algorithm; scale-space extrema, keypoint localization, orientation assignment, and keypoint descriptor[27].

The first stage, scale-space extrema detection, scans the entire image using a difference-of-Gaussian filter to find potential keypoints. To determine these keypoints, a training image is convolved with a variable-scale Gaussian blur. Equation (1) is the basis of the Difference of Gaussian implementation, which results in a data set of the strongest possible keypoints.

$$D(x,y,\sigma) = L_1(x,y,\sigma_1) - L_2(x,y,\sigma_2) \tag{1}$$

$$L_i(x,y,\sigma) = G(x,y,\sigma_i) * I(x,y) \tag{2}$$

$$G(x,y,\sigma) = \frac{1}{2\pi\sigma^2} e^{-(x^2+y^2)/2\sigma^2} \tag{3}$$

Equation (2) specifies that either right or left image can be used as the training image; where * is the convolution operator in the x and y region, $G(x,y,\sigma)$ is the Gaussian blur and $I(x,y)$ is the training image. The resultant $D(x,y,\sigma)$ is the aforementioned database populated with likely keypoints for future matching.

Next, keypoint localization fits a model to determine location and scale of every possible keypoint. By looking at nearby locations, scales, and ratio of curvatures; keypoints sensitive to noise can be eliminated as possible future matches. Subsequently, the orientation assignment stage maximizes the likelihood of matching and recognition by assigning a consistent orientation vector to each keypoint. The consistency of the orientation allows for an increased change of a match. Features that maintain similar orientation vectors, between two images, usually indicate invariance to rotation or translation, thus a higher probability of a mach. Lastly, the keypoint descriptor measures the local image gradients in order to allow the maximum allowable tolerance when matching with a test image[13]. A final thresholding filter is used to eliminate matches outside of the limits. SURF relies on the same principles as SIFT but is considered a more robust and faster version. One major difference between the two is SURF's use of square filters to approximate Gaussian smoothing, which reduces on computational time[8]. Depending on the robustness of the thresholding parameter initiated before using either algorithm, SURF can be as much as three times faster than SIFT when matching between images[28].

SIFT and SURF have distinct advantages over other feature detection algorithms. While SIFT is more computationally demanding than SURF, both are robust enough to not solely rely on edge or corner detection. These algorithms also find keypoints based on illumination and curvature that other detection or matching algorithms will not take into consideration. The threshold filter set for keypoint acceptance allows for even more robust usage when dealing with limited resolution. Since the NanEye only has a resolution of 250 pixels (W) by 250 pixels (L), SIFT and SURF are able to determine matches that other algorithms are unable to identify. In Figure 1.2, the stereo pair is displayed and each matched point corresponds to a line drawn between the two images. The combination of SIFT and SURF was able to match over 100 distinct features in a limited area.


All SIFT/SURF Matches

Figure 1.2: Total SIFT and SURF matches found on an objects surface.

As with any feature matching algorithm, not every pair of matches is necessarily accurate. There are two distinct types of incorrect matches which must be identified and removed; false positives or mismatched features. Additionally, because SURF is based on the original principles of SIFT, there will be repeating results that must be eliminated. A false positive match occurs when SIFT and SURF recognize two features that are similar to one another yet are not true matches. This usually results from an illumination disparity or contour shade in the image. The resulting incorrect coordinates can be up to 5 or 6 pixels off from the correct image coordinate. These errors are much more difficult to detect due to seemingly correct matches both from eye test and from relative position on the image. These errors are not detected until the 3D reconstruction stage where the triangulated 3D coordinates are physically impossible to have occurred.

The second type of error that occurs is a complete false match. This occurs when two features have enough mathematical similarity to fall within the tolerance level but in reality are displaying two distinct features. Features that are very similar to one another but lie on opposite sides of the images can be misidentified as matches. Usually this occurs when looking at highly patterned surfaces which contain a high degree of symmetrical designs.

To correct for false matches a simple test was run on all the matches. Since the cameras are placed on the same axial plane as one another, matches must lie along the same horizontal line. The horizontal coordinate of the matched feature on the right image was compared to the horizontal coordinate in its counterpart on the left. If the coordinate's difference was outside of an acceptable threshold, they were removed as false matches. Figure 1.2 shows that among all 100 matches, some are indicating two features that cannot be a match. One example is the match indicated by the red line at the bottom of Figure 1.2. That match corresponds to two different areas on opposite sides of the object and thus cannot be a true match. Upon removing all the mismatched features and double matches a smaller number of matches exist, but are more likely to be true matches. Figure 1.3 shows the results after running a horizontal test check and removing all doubles, where there are now over 40 distinct matches.

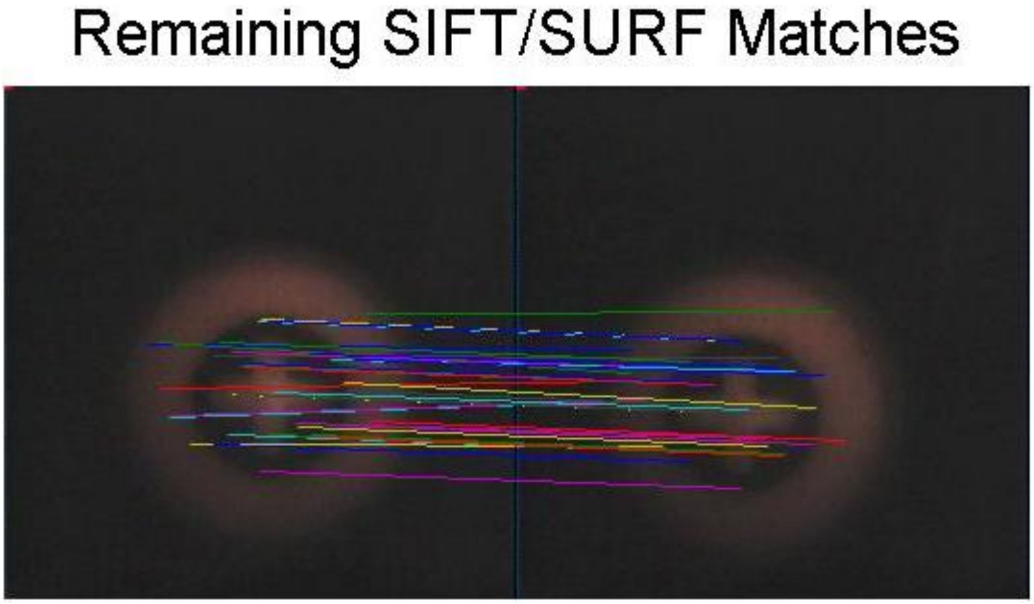

Figure 1.3: Remaining SIFT and SURF matches after false positives, incorrect matches, and double matches are removed

1.3 Triangulation

Mapping coordinates from real space onto an image and from and image to real space generally involves linear algebra and geometry. A simple example of mapping 3D coordinates onto one of the image planes is given by the equation below.

$$m = \boldsymbol{C} * M \tag{4}$$

Here, m is the matrix of the x-y coordinates on the image, **C** is the camera projection matrix and M is the x-y-z coordinates in real space. Equation (4) shows the mathematical equation needed to map real world coordinates to image coordinates. Triangulation is the reverse of this problem and far more complex. Triangulation is based on epipolar geometry; where a pair of stereo images is used to triangulate a common point between each image in the 3D world[29]. Figure 1.4 diagrams the basis of this geometric relationship. A line from each point, O_L-P and O_R-P, in the two images intersects somewhere in real space, P.

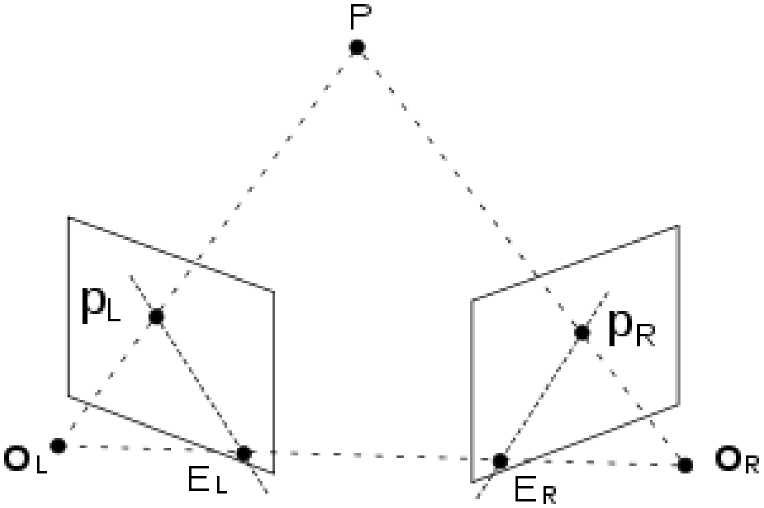

Figure 1.4: Epipolar Geometry Diagram. The basis for triangulation. This diagram outlines the fundamental geometric properties that for the basis of triangulation.

Here, two images view the same scene with optical centers at O_L and O_R. Point P is imaged onto the left and right images appearing as p_L and p_R, respectively. A ray can be drawn from O_L-P as well as from O_R-P, where the intersection of these rays is point P in real space. In order to solve for point P in terms of real world coordinates a triangulation equation was determined[30].

$$P \sim \tau(P_L, P_R, C_L, C_R) \tag{5}$$

Equation (5), states that given images coordinates, P_L, P_R, from two images as well as the two camera matrices, C_L, C_R, than it is possible to triangulate the image point P in real space. Depending on the computational method used, τ, can vary in its implementation. For the purposes of this work τ represents a method using single value decomposition (SVD) to determine the unitary matrix for the inverse of the two system problem based on Equation (4).

In order to maximize the accuracy of the triangulation results, lens distortion had to be eliminated from the images. For the case of the NanEye, barrel distortion is the most significant type of aberrations that occur. Barrel distortion is an effect that causes images to seem inflated, specifically in the center and radiating outward. This type or distortion usually comes from wide angle lenses and is due a mismatch in size between lens and sensor size. To adjust for this distortion, the correct coordinates are computed by a translation to the optical center and then normalizing by the focal length, in pixels. A custom algorithm was written to correct the distortion once and save the camera parameters for automatic correction in the future. Figure 1.5 presents the results, where the image on the left is the uncorrected image of a checkerboard and the image on the right is the corrected one. It is important to observe that the checkerboard on the left appears to be curved while the one of the right does not.

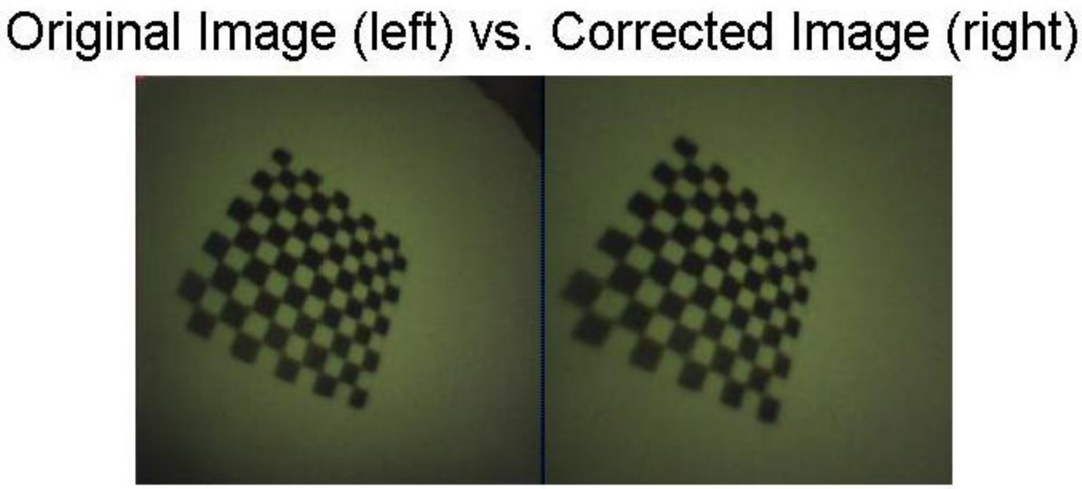

Figure 1.5: Comparison or two images, left displays the raw image without any sort of aberration correction. The one on the right shows the same image after the lens distortion correction.

While distortions in lenses as well as incorrect point matches can cause errors, because triangulation requires only elementary matrix manipulation (linear algebra) it is still one of the fastest and most effective ways to gain 3D information from a pair of stereo images.

1.4 Results

When all three methods are combined; stereo vision, feature matching, and triangulation, every matched point between the two images can be given as 3D coordinates relative to one of the cameras. A mount for both cameras to remain locked in place was 3D printed, with a diameter of 7.0mm with a camera separation of 4.0mm, as seen in Figure 1.6. The NanEye was connected to a propriety evaluation board which in turn connected to a computer via USB cable. The image capture software was a propriety user interface from AWAIBA, which allowed capturing of simultaneous frames. Processing and all subsequent results were carried out on a Toshiba Qosmio X775 laptop (2.2GHz, 8.0 GB RAM) which ran Matlab 2013b (Mathworks).

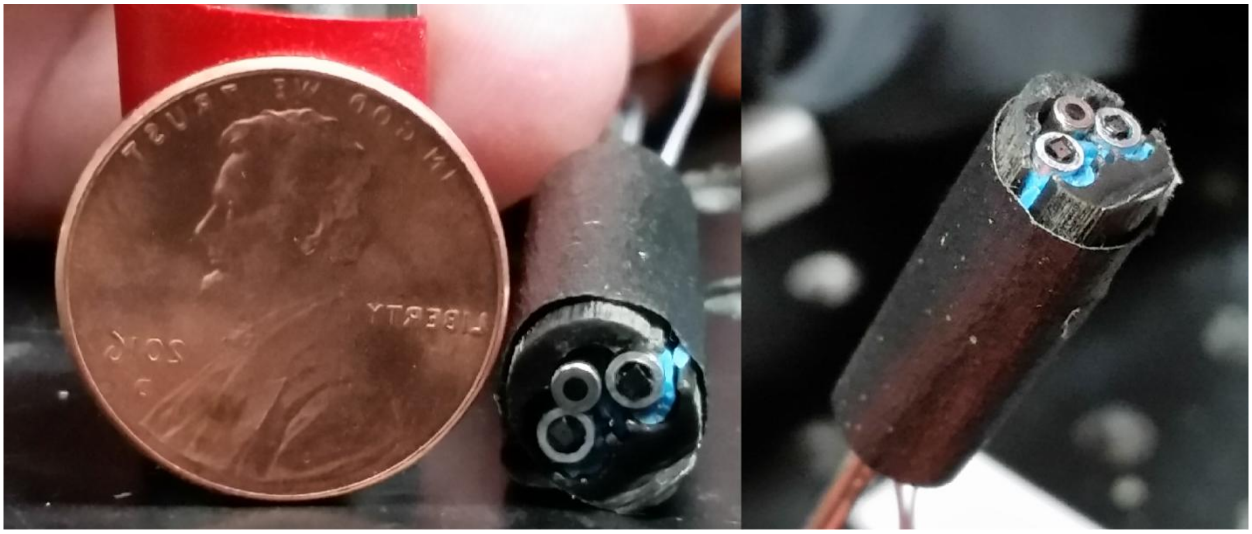

Figure 1.6: Views of the probe after completion. Two NanEye cameras placed 4.0mm apart with a optical fiber which runs along the center track.

In order to compare this device with established endoscopes, the results from the validation had to be on roughly the same order as other 3D endoscopic devices. One such device implementing a structured light approach was characterized as having a 3D resolution of 100μm[11]. While the approach of using structured light yields high resolution, it does involve a significant amount of processing and hardware. The goal here was to reach the same level of accuracy while using a much less complicated system.

The first characterization that was preformed was of the resolution of the NanEye cameras. Figure 1.7 displays the results from the USAF Resolution target that was used determine the resolution of the camera both in Line-Pairs and Microns. By determining the resolution it was possible to approximate the resolution for triangulation results. The 1951 USAF Resolution Test Chart was developed to determine the resolution of optical imaging, consisting of two groups with three vertical and horizontal bars descending in size. As the group number increases, while the bars decrease in size, the resolution is said to become higher. Using a 1951 USAF Resolution Test Chart, multiple images were taken using the NanEye over a range of distances. In order to validate the results, custom made a spatial domain algorithm was implemented to differentiate from individual line pairs. This algorithm looked for the discrepancies between the white background and the black bars. If there was no interference from the black bars between each line pair than it was said the group was resolvable. The analysis was performed on both the distorted and undistorted images to determine the severity of the lens distortion.

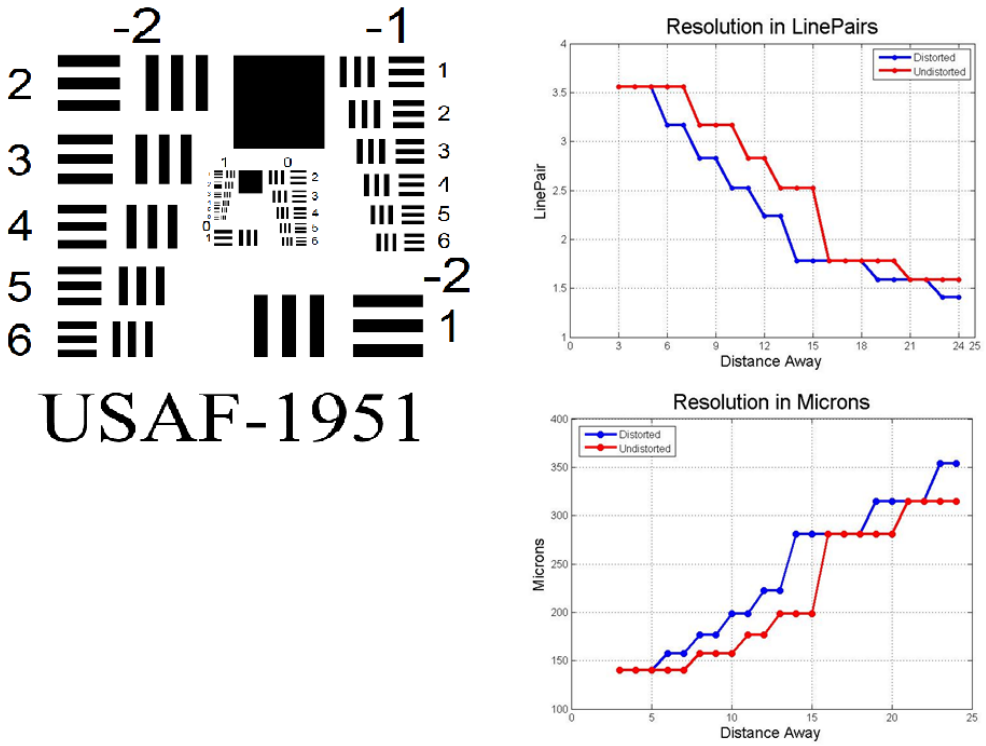

Figure 1.7: US Air Force Resolution Test chart, along with two plots of the resolution. The top graph displays the resolution in terms of Line Pairs while the bottom graph displays the resolution in microns

These results showed the NanEye have a maximum resolution of 140.31 microns at a distance of 3.0 millimeters away and a minimum resolution 353.55 microns at a distance of 24.0 millimeters away. These results indicate that the NanEye would be able to distinguish features on the order of several hundred microns within these distances. Distinguishing features at this resolution indicates that the triangulation results should be roughly on the same magnitude. It should also be noted that the resolution may have been higher at closer distances, if the USAF Resolution Test Chart had a more groups for higher resolution test. However, the established resolution was sufficient for the applications addressed in this work, thereby not making it a necessity to use a different target. Tables 1.1 & 1.2 depict the results of the resolution test for both the distorted and undistorted images.

Distance Away	Resolution Distorted (Lp/mm)	Resolution Distorted (μm)	Distance Away	Resolution Distorted(Lp/mm)	Resolution Distorted(μm)
24	1.41	353.55	13	2.24	222.72
23	1.41	353.55	12	2.24	222.72
22	1.59	314.98	11	2.52	198.43
21	1.59	314.98	10	2.52	198.43
20	1.59	314.98	9	2.83	176.78
19	1.59	314.98	8	2.83	176.78
18	1.78	280.62	7	3.17	157.49
17	1.78	280.62	6	3.17	157.49
16	1.78	280.62	5	3.56	140.31
15	1.78	280.62	4	3.56	140.31
14	1.78	280.62	3	3.56	140.31

Table 1.1: The results the NanEye resolution at each tested difference with the distorted images.

Distance Away	Resolution Undistorted (Lp/mm)	Resolution Undistorted (μm)	Distance Away	Resolution Undistorted (Lp/mm)	Resolution Undistorted(μm)
24	1.59	314.98	13	2.52	198.43
23	1.59	314.98	12	2.83	176.78
22	1.59	314.98	11	2.83	176.78
21	1.59	314.98	10	3.17	157.49
20	1.78	280.62	9	3.17	157.49
19	1.78	280.62	8	3.17	157.49
18	1.78	280.62	7	3.56	140.31
17	1.78	280.62	6	3.56	140.31
16	1.78	280.62	5	3.56	140.31
15	2.52	198.43	4	3.56	140.31
14	2.52	198.43	3	3.56	140.31

Table 1.2: The results the NanEye resolution at each tested difference with the undistorted images.

Next, the accuracy of the triangulated coordinates were characterized. In order to accomplish this, several tests were performed with an object at fixed distances away from the cameras. A region of interest (ROI) was selected on the object and the computed depth coordinates were compared to the known measured distances. Additionally, large distinguishable features were measured on the object and their length was then computed from the computed 3D coordinates. Figure 1.8 shows an example of a sample image acquired, indicating a segment that was calculated and then measured. These comparisons were used to validate the accuracy of the depth as well as the XY-axis, respectively. Table 1.3 shows the results and error calculations for the accuracy tests carried out using the device.

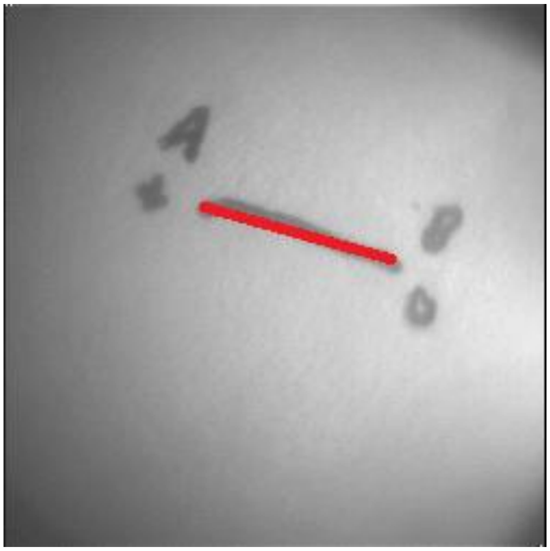

Figure 1.8: Example of object used to determine both the depth and the distance between two points. The calculated distance is displayed by a red line in the image. A flat object with letters and symbols were used to generate matched points between the stereo pair. All matched features were used to compute the depth of the flat object relative to the cameras. Two triangulated coordinates, at the beginning and ending of the line, highlighted in red, were used as spatial coordinates to determine the length of the line.

Distance away from probe	Z-axis calculated (mm)	Z-axis actual (mm)	Z-axis % Error	XY-axis Calculated Length (mm)	XY-axis Measured length (mm)	XY-axis Length % error
10mm	12.10	12.0	0.8	6.42	6.33	1.4
15mm	15.25	15.0	1.6	7.05	7.57	6.9
25mm	24.50	25.0	2.0	10.55	11.43	10.7

Table 1.3: Results from the dimensional validation

From Table 1.3 the errors and accuracy of the 3D coordinates are established. Depending on the distance from probe to object, the Z-axis accuracy could be as little as 100μm. This result held true for the XY-axis results, where, at the same distance the calculated length of the features was 90μm. Comparing these results against other methods for computing quantifiable 3D measurements using an endoscope, it is clear that this stereoscopic system can yield 3D measurements on the same magnitude as those techniques.

Finally, utilizing the 3D coordinates gained from imaging a person's knuckle and placing the probe 20mm away, a surface plot was created with an overlay of the ROI. A knuckle was used as a test object due to the high number of feature that could be discerned and matched given its physical structure. Without a protocol to insert this into a live, human subject, using a body part outside the body was deemed prudent to be able to determine how well the cameras could image live tissue. In order to create a continuous surface plot, data points between matched features were extrapolated using a three point averaging approach. The surface plot in Figure 1.9 displays a cross section of the knuckle as well as the depth. In this case the ROI selected was a 15mm by 15mm section of their knuckle. The calculated length and width of the ROI turned out to be 13.7 (L) by 13.39 (W), which is an percent error of 8.6 % and 10.7% respectively. While the NanEye posses significantly reduced resolution compared to more conventional devices, the accuracy at quantifying dimensions and depth were comparable to these devices. With simple off the shelf sensors and basic computer vision algorithms, it is possible to achieve a device that has equal or better 3D resolution than more established devices such as the 3D endoscope using structured light or a dual aperture system.

Figure 1.9: Surface plot with the ROI overlaid on top. The image on the left is the view from the front while the image on the right is at an angle to display the depth reconstruction of the knuckle.

Chapter 2: Laser Speckle Contrast Validation

Over the last 20 years laser speckle contrast imaging (LSCI) has emerged as a very useful tool for full-field imaging of blood flow. Recently, LSCI has received significant attention due to its use in *in-vivo* studies of the brain. During this period, many different approaches and devices have been used to increase the use of LSCI. The work described in the following chapter details the validation of the NanEye cameras for use in LSCI.

2.1 Theory

Laser speckle imaging (LSI) is the process of analyzing the random interference pattern created when coherent light scatters off of a turbid medium. Speckles are created when coherent light is scattered off of a medium and a random interference pattern is seen. Due to coherent light scattering on the medium at different positions, a sensor will detect the difference in distance traveled as constructive or destructive interference. The combination of this interference is called a “speckle pattern”[31].

A speckle pattern will vary depending on the type of medium coherent light scatters off of. If coherent light scatters against a static medium, than the intensity differences seen by the sensor will change slowly. Oppositely, if the medium is dynamic, than the interference pattern will be constantly changing and the subsequent intensities from the interference pattern will fluctuate[32]. In areas with higher dynamic flow rates, the intensity fluctuations happen faster as opposed to lower flow rates where the intensity fluctuations are slower. These intensity fluctuations result in the appearance of blurring in the speckle pattern. The degree of blurring can be analyzed and the resulting image is known as a speckle contrast image. In order to create this speckle contrast image, the raw speckle image can be processed in one of two way; spatially or temporally[23].

$$K_s = \frac{\sigma_s}{<I>} \tag{5}$$

In equation (5), K_s is the resulting spatial contrast value, σ_s is the spatial standard deviation of pixel intensity, and $< I >$ is the mean intensity of the pixels. Alternatively, the temporally processed contrast value results in K_t and σ_t, where t denotes the temporal contrast and standard deviation of the pixels. The size of individual speckles is dependent on several variables as seen in Equation 6, where λ is the wavelength of light, M is the magnification of the lens, and $f/\#$ is the f-number of the system. In order to effectively sample the speckle pattern the minimum speckle diameter,$\rho_{speckle}$, should be at least twice the size of the sensor's pixels. This requirement is known as the Nyquist sampling criteria[33].

$$\rho_{speckle} = 2.44\lambda(1 + M)f/\# \tag{6}$$

2.2 Background

The need for minimally invasive blood flow measurements has grown over the past few decades. LSCI has provided an outlet for this need. A large amount of research has been spent developing ways to use LSCI in live subjects both in humans and animals.

One of the earliest uses of LSCI was the monitoring of skin profusion, due to its abundance and superficial depth[23]. This application does come with inherent obstacles. Skin perfusion is difficult to monitor because most of the blood vessels exist under a layer of tissue. This complication generally means that measuring a single vessel is almost impossible to quantify but it does allow for measuring of overall skin perfusion on the capillary level. While this obstacle places a limitation on the application of skin profusion, recent work has been done to determine the effectiveness of laser therapy on skin treatments[34]. Another area of research on both humans and animals was the use of LSCI to measure blood flow in the retina[35]. Instead of computing normal speckle contrast, a new measure called normalized blur (NB) was developed based on the existing principles of time integrated speckle intensity. The main reason why this area of research was furthered was due to the accessibility of the eye as well as how relevant retinal blood flow is to ophthalmological diseases. Unfortunately, most of the work done around retinal blood flow was not performed on humans because of the limited spatial resolution for the sensor. Most applications of *in-vivo* LCI have been used to measure the blood flow in an animal cortex, specifically rats and mice. Due to the high resolution of modern cameras, highly resolvable spatial maps of blood flow can be created over very small regions of the brain. These maps, allow for the analysis of relative blood flow while remaining minimally invasive. Usually, a portion of the skull or a layer of skin is removed to access an area of interest. This application has been used for monitoring functional brain activation, cortical spreading depression, or pathology of strokes[23]. Not only has work been done on different physiological sites of the body but there has been significant work done with using off the shelf components as well. With the amount of low cost and high resolution web-cameras available, these devices have been introduced into the clinical world of LSCI[36]. This is the first step toward creating a low cost LSCI system that could eventually become portable. The goal to create portable low cost devices for LSCI would be to image areas of the body that were previously inaccessible.

2.3 Obstacles overcome

Two major limitations in conventional LSCI, which the NanEye potentially can solve, are the dependence on high resolution sensors or the lab grade setup required to achieve results. The higher the resolution, the larger the spatial window for processing is. Also, more pixels generally means there are more values that can be averaged in a smaller ROI. This can lead to more stable results if the regions of interest have small dimensions. Convention cameras used in LSCI, off-the-shelf or not, are too large to image inside the body while maintaining a minimally invasive approach. In order to reach these less accessible areas, smaller cameras must be implemented. The downside to a smaller camera is the obvious loss in resolution and the potential loss in magnification or f/#. Smaller magnification or f/# will result in a decrease of speckle diameter seen from Equation 6. One of the main focal points of this work was to overcome the side-effects of using smaller cameras, at the same time establishing the NanEye cameras as a valid means to measure speckle contrast data. In order to achieve this, certain obstacles of the NanEye had to be overcome; vignetting, reduced resolution, and reduced f/#.

There are four types of vignetting which will result in the decrease of brightness in an image, beginning at the edges and corner; mechanical, optical natural and pixel. Mechanical and optical vignetting occurs due to a blockage of the light rays entering the aperture. This blockage can occur from a physical dimension of the external camera housing, as is the case with mechanical. In optical vignetting, the blockage stems from a mismatch of multiple optical elements leading to a reduced lens opening for off-axis light. Natural vignetting occurs from a falloff due to the “cosine forth” law of illumination. This falloff in intensity is related to the angle that the light rays contact the sensor and the fourth power of cosine. Pixel vignetting is specific only to digital images, where angle dependence light is received and processed at different intensities.

The NanEye is affected primarily by mechanical vignetting, due to its high field of view, 120 degrees, and its 1mm x 1mm casing. This combination, high field of view and small casing dimensions, causes the exterior of the image, corners and edges, to appear darker as seen in Figure 2.1. Comparing a single raw frame of data between the NanEye and Chameleon, the Chameleon does not suffer from the same radial decrease in intensity the same way the NanEye does. This uneven intensity distribution can cause significant problems when processing the raw speckle data. The concern with the vignetting is the loss of information around the edges and the corners of the image. Since the NanEye already has low resolution, 62.5K, additional loss of usable image, could be detrimental to the results or future work.

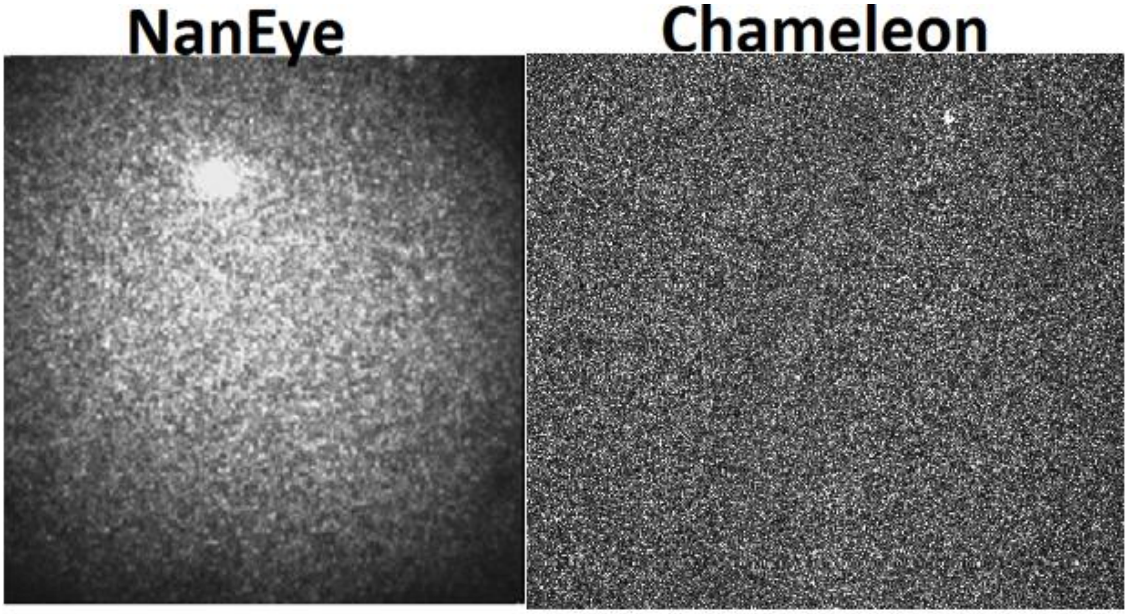

Figure 2.1: A comparison between the NanEye (on the left) and the Chameleon (on the right). The effects of vignetting are displayed. The NanEye which suffers from vignetting, has non-uniform intensity, specifically around the edges. The Chameleon, which does not suffer from vignetting has a uniform intensity throughout the image

Another major obstacle to overcome was low f-number of the lens in the NanEye camera. These devices come pre-packaged with the sensor and optics and once the device is fabricated the optics cannot be changed. The largest f-number for any of the NanEye variations was 2.8. As seen from Equation 6, the diameter of speckles has a direct relationship to f/#. In order to achieve optimal sampling criteria, the minimum speckle sizes should be at least two times the size of pixel size. This is to ensure that multiple pixels are able to image one speckle.

2.4 Results

As previously mentioned, little to no work has been done using cameras with limited resolution in the LSCI world. This is mainly due to the numerous obstacles needed to overcome this as well as the lack of immediate need for cameras small enough to be placed inside the body. In order to establish that the NanEye cameras are viable devices to be used in LSCI a validation study was performed. This study had two parts to it; an *ex-vivo* flow phantom study and an *in-vivo* hyperemic response study. In both cases results were compared to an existing lab-grade Point Grey Chameleon USB 2.0 CCD, attached with a LMH-10X lens (Computar). For the flow phantom study, contrast values from the NanEye and Chameleon were compared against one another and a statistical analysis was performed to determine if there was any significant difference between the results. Alternately, a sensitivity measurement was taken for the hyperemic response study and the resulting values were compared against one another. The results from these comparison studies properly characterize the NanEye for its application in LSCI.

For the flow phantom study a 1% solution of Intralipid (Fresenius Kabi) was pumped through a flow phantom using a syringe pump (Harvard Apparatus) at variable speeds. These speeds ranged from 1.0 mm/sec 7.0 mm/sec by increments of 0.5 mm/sec, with two extreme cases of .05 mm/sec and 15.0 mm/sec. The flow phantom was circular with a diameter of 87mm and a capillary tube embedded at the surface level with a diameter of 0.68mm. The laser, an 808nm 150mW laser (Oxdax), was stationed at a fixed height, 220 mm away from the phantom. In order to overcome the smaller f/# of the NanEye and achieve the Nyquist criteria, the Ondax 808nm laser was chosen to increase the minimum speckle diameter given by Equation 6. Both the AWAIBA NanEye and the Point Grey Chameleon were placed at a fixed distances above the phantom. Since the NanEye has substantially lower resolution and shorter working distance it was placed substantially closer to the phantom, 30mm, as opposed to the Chameleon which was placed about 250mm above the phantom, as seen in Figure 2.2.

2.3.

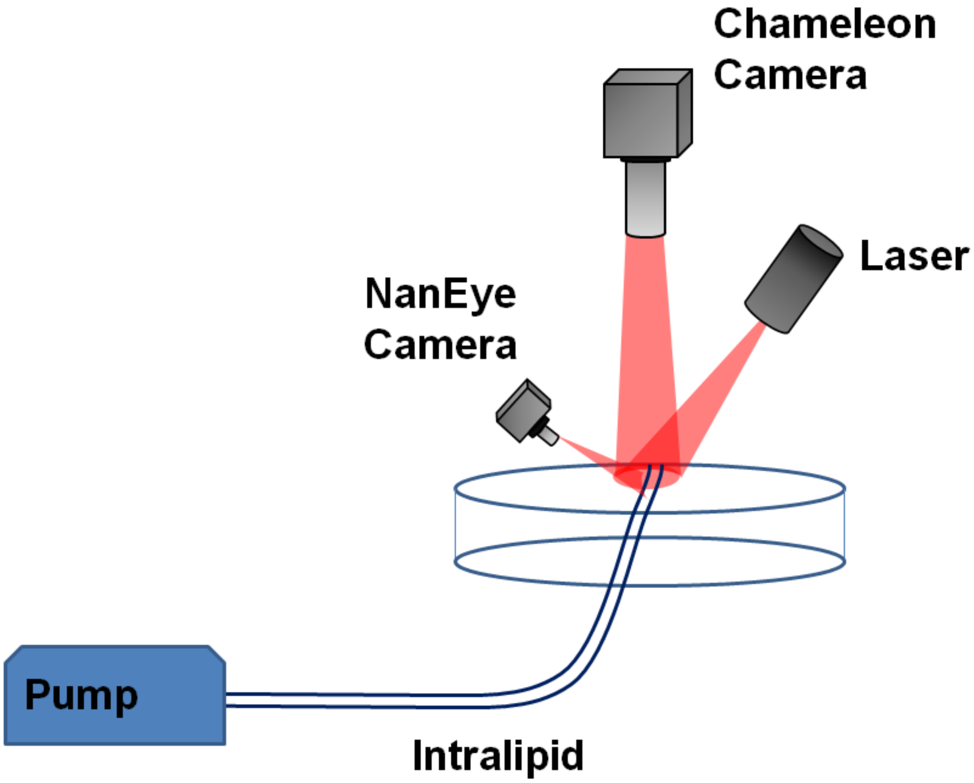

Figure 2.2: Diagram of the flow phantom experiment. Both the NanEye and Chameleon simultaneously acquire data while intralipid is pumped through the tube.

During each flow rate, the pump was given enough time to reach equilibrium before data was acquired. For both cameras 5 seconds of video was taken, resulting in 225 frames for the NanEye and 75 frames for the Chameleon. Each video was broken down into its individual frames and stored for processing later on. To compute the speckle contrast, 25 frames from the NanEye and Chameleon were taken and spatially processed. A 3 x 3 sliding window was used to minimize the loss in spatial resolution on these frames. All 25 spatially processed contrast images were subsequently averaged together in order to gain a higher signal to noise ratio[37]. The resulting contrast images were converted to gray scale to better differentiate between flow sections and static phantom section, shown in Figure 2.3.

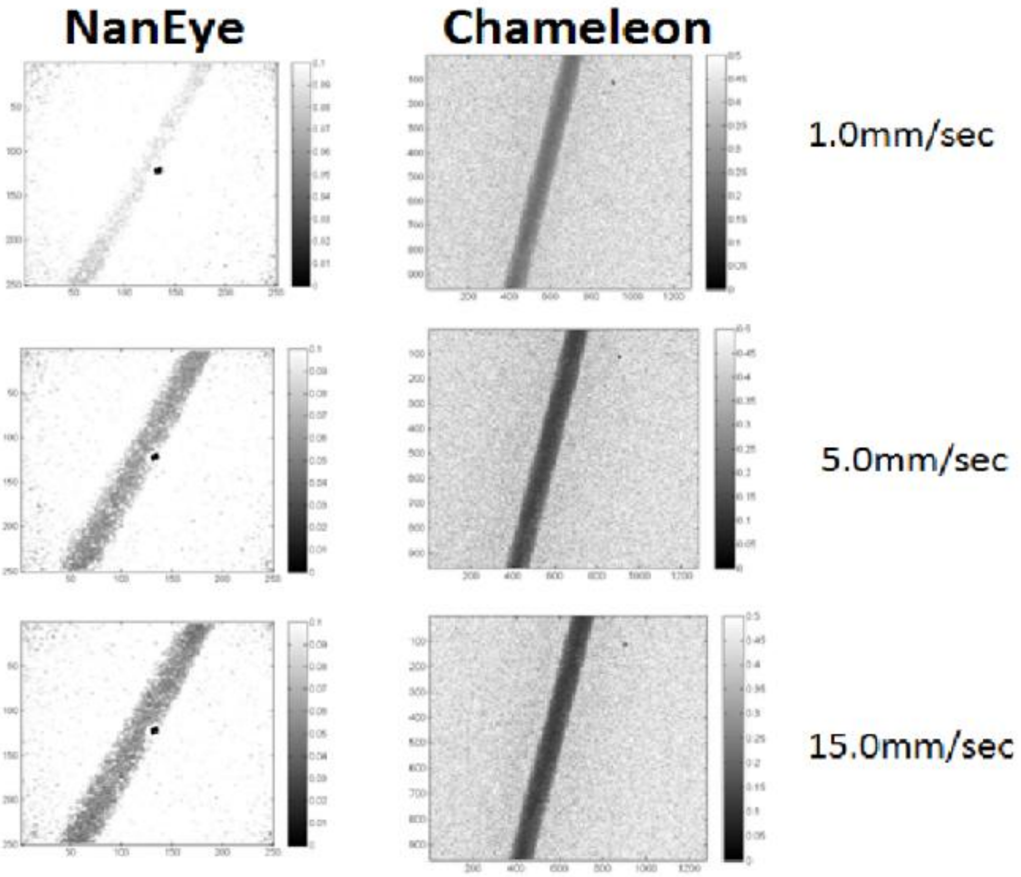

Figure 2.3: A side by side comparison, between the NanEye and Chameleon, of the changes in speckle contrast images as the flow rate is increased10

Figure 2.3 depicts, in descending order, an increase in flow rate for both the NanEye and the Chameleon. The left column displays the NanEye contrast images while the right column is the Chameleon contrast images. In both columns, as flow is increased from 1.0 mm/sec to 15.0 mm/sec the tube running through the center gets darker. This darkening is a decrease in the speckle contrast and is the expected result from an increase in flow rate.

In order to quantify the dynamic range of the NanEye over the flow rate, a ROI was selected at the center of the tube. For the case of the NanEye the ROI was chosen away from the dark spot seen in Figure 2.3 at the center, which is specular reflection and not true contrast data. The ROI for the NanEye was a 10 x 10 block of pixels and a 30 x 30 block for the Chameleon. The larger ROI for the Chameleon was chosen to maintain a similar ratio of ROI to image as in the NanEye. The contrast values inside the ROI were averaged together and plotted, shown here in Figure 2.4.

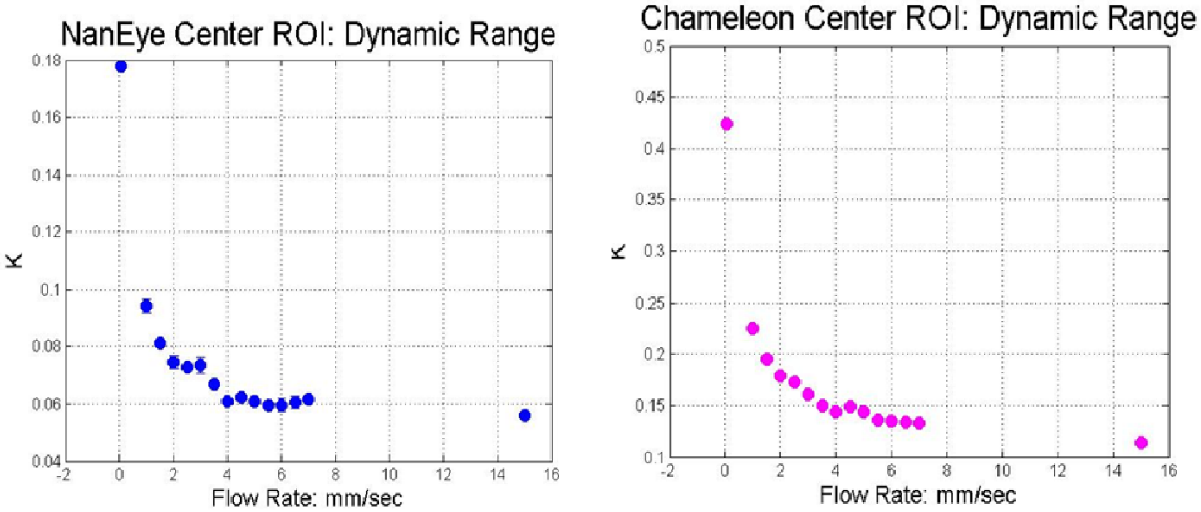

Figure 2.4: Plots of the speckle contrast taken from center ROI where the vignetting effects the NanEye the least

Both the NanEye and the Chameleon appear to display the same exponential decay in speckle contrast while the flow rate is increased. Figure 2.4 shows the difference in dynamic range between the NanEye and the Chameleon. While the NanEye has a higher variation in contrast compared to the Chameleon, this is likely caused by the higher resolution of the Chameleon and the larger ROI selected. The Chameleon does have a higher dynamic ranging, beginning at 0.42 and dropping off to 0.12, over the same span that the NanEye drops from 0.17 to 0.059. A direct comparison of these two distributions cannot be done in their present state. In order to accomplish this, both sets of data were normalized against the maximum and plotted together. Figure 2.5 indicates that the relative changes in dynamic ranges between the two cameras were nominal.

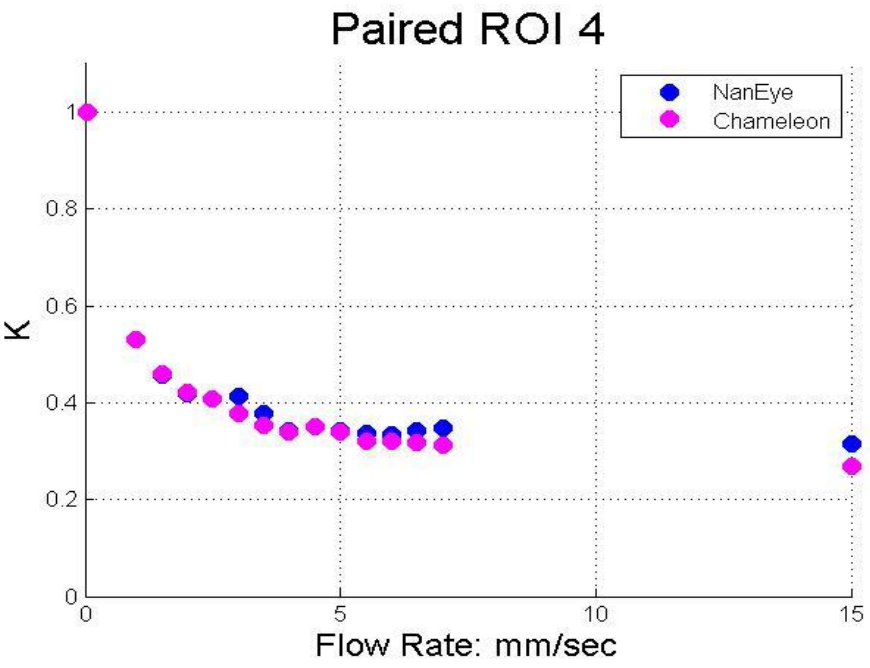

Figure 2.5: Speckle contrast for both the NanEye and the Chameleon when both data sets are normalized against the max.

Due to the issue of vignetting discussed earlier, a wider sampling of ROIs was needed. To properly determine the effect the vignetting had on the speckle contrast, multiple ROIs were chosen along the tube. The new ROIs were processed with the same technique as before and plotted to see the effect of the vignetting on the contrast. Figure 2.6 shows the new ROIs selected, the plots of the raw contrast points as a function of flow rates, and all the normalized ROI data.

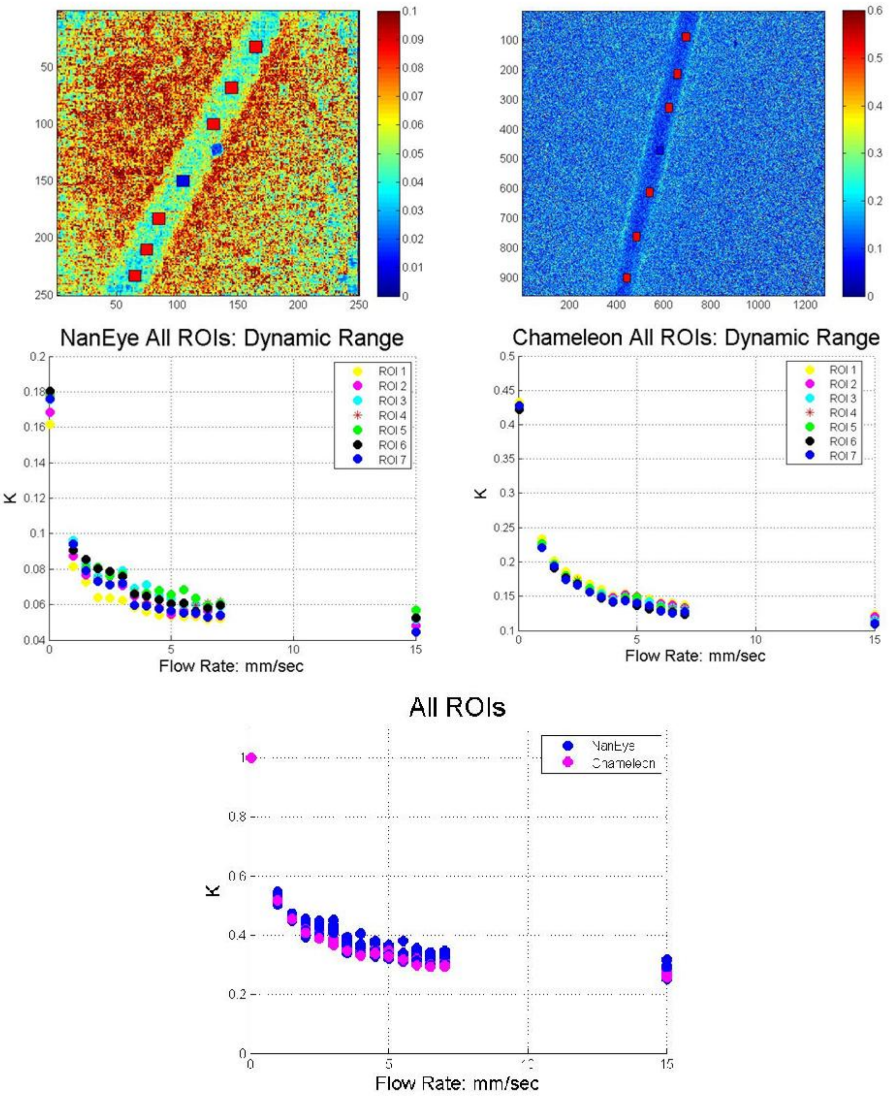

Figure 2.6: Display of all the ROIs taken along to tube. Second row is the raw speckle contrast values for each ROI and the final row is all normalized sets plotted on the same axis.

From the second row in Figure 2.6, the side effects of the vignetting are clearly apparent in the raw data. Unlike the Chameleon, whose multiple ROI data points have little variation along the tube, the NanEye ROIs are more dispersed. Even in the plot of the normalized data, the Chameleon data points lay almost on top of one another while the NanEye still remains dispersed. In order to quantify this difference and determine whether this dispersal creates a significant issue in the data, a Wilcoxon rank sum test was performed on the normalized data sets between each ROI for the NanEye and the Chameleon. Table 2.1 shows the results of this statistical analysis.

	Chameleon ROI 1	Chameleon ROI 2	Chameleon ROI 3	Chameleon ROI 4	Chameleon ROI 5	Chameleon ROI 6	Chameleon ROI 7
NanEye ROI 1	0.694	0.820	0.852	0.950	0.917	0.694	0.633
NanEye ROI 2	0.983	0.787	0.756	0.663	0.663	0.351	0.395
NanEye ROI 3	0.395	0.309	0.351	0.254	0.272	0.141	0.101
NanEye ROI 4	0.820	0.604	0.604	0.520	0.548	0.178	0.152
NanEye ROI 5	0.309	0.221	0.254	0.165	0.165	0.078	0.093
NanEye ROI 6	0.983	0.787	0.787	0.694	0.663	0.395	0.372
NanEye ROI 7	0.372	0.494	0.520	0.520	0.787	0.983	0.852

Table 2.1: Results from the Wilcoxon Rank sum Statistical analysis for every ROI.

The entries for Table 2.1 are the resulting p-value from the rank sum statistical analysis. Each ROI in the NanEye was tested against each of the Chameleon ROIs. The diagonal entries, highlighted above, correspond to an ROI tested against its mirror on the opposing image. With an average p-value of .7620, for every permutation, there is no statistical significant difference among ROI selection. Although vignetting does cause some deviation in the data, it is not significant enough to alter the underlying distribution and outcome of the contrast data.

Finally, hyperemic response study was performed to determine if the NanEye had comparable sensitivity during in-vivo measurements. This occlusion follows the work of Yang et. al.[38] and performed a 390 second occlusion; 30 seconds of baseline, 240 seconds of full arm occlusion, followed by 120 seconds of release. During this time, both the NanEye and the Chameleon were positioned to image the fingers of the patient. A 15 frame sliding temporal algorithm was used to process both sets of data. Figure 2.7, shows the plots of the contrast versus time during the entire experiment. In order to determine sensitivity, a calculation was made following the work done by Dunn et al [39]. Here sensitivity is determined as the as ΔK/K, where ΔK is the change in maximum contrast and

K is a baseline measurement. Figure 2.7, displays the results from the three patients the study was performed on.

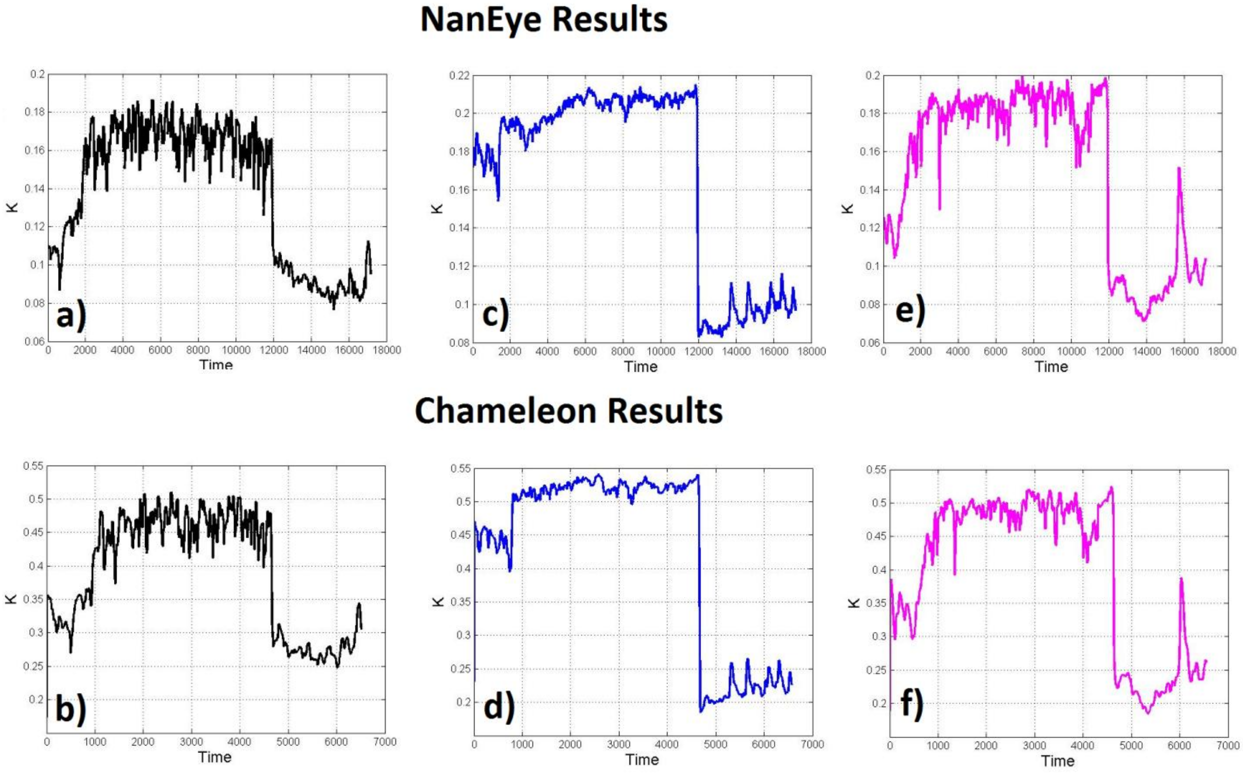
NanEye Results

Chameleon Results

Figure 2.7: Results from the hyperemic response study. The top row displays the three patients data for the NanEye while the bottom row displays the same for the Chameleon.

The NanEye yielded sensitivities between .64, .98, and 1.04 for all three subjects. While the Chameleon yielded a range from .61, 1.06, and 1.18 for the same three subjects respectively. While the sensitivity measurements vary from patient to patient, it was determined that the sensitivity between the NanEye and the Chameleon was within acceptable limits. A standard two sample T-Test was performed on the results and yielded a p-value of 0.56. The results from the hyperemic response study and the flow analysis can be concluded to say the NanEye camera has enough sensitivity to detect physiological changes in speckle contrast similar to standard lab-grade cameras.

Chapter 3: Co-Registered 3D Speckle Surface Map

The primary goal of this project was to create an endoscopic probe that provided multiple imaging functionalities in a single device and met standards set by current technologies. By combining 3D triangulated measurements with blood flow analysis in one probe, the number of devices traditionally used to gather such data was reduced. The secondary goal was to maintain a high level of accuracy and sensitivity for both functionalities. While the sensors used in this probe were smaller and had a lower resolution, the prototype still managed to achieve a similar accuracy and sensitivity as existing systems. This is a step forward in endoscopic functionality.

The NanEye camera has rather small dimensions. It is only 1.0mm by 1.0mm allowing for the placement of two cameras inside the probe. Given the diameter of the probe, 7.0mm, there was sufficient tolerance for proper separation needed to obtain 3D data. Additionally, an optical fiber was placed between the NanEye cameras to deliver illumination for both the imaging techniques. By keeping the overall diameter at 7.0mm, the probe maintains current dimensional standards as other 3D endoscopic devices. As discussed previously, the use of stereoscopic imaging is computationally less demanding than other 3D imaging modalities. This demand is further lessened due to the low resolution the NanEye possesses. Lower resolution also means less time needed to search for matches, triangulate coordinates, and reconstruct 3D surface plots.

This project also presents one of the first cases where sensors of this scale, specifically the NanEye cameras, were validated to be used for LSCI. This expands the areas in which flow can be analyzed using LSCI. With sensors this compact, it is now feasible to insert them inside the body to access regions of flow that were previously inaccessible to conventional LSCI setups.

The combination of both these functionalities in one device allows for flow analysis to be paired with 3D surface plots. Specifically, this would allow for flow to be tracked inside the body down long cavities. This would result in combining a determined distance to regions of interest pertaining to areas of flow. It would also provide the ability to quantify extent of blood flow throughout the internal cavities of the body with dimensional analysis. This could be of use to surgeons as a method to minimize the tissue excised during a biopsy or to evaluate the extent of an abnormal growth surrounded by areas of blood flow.

One of the primary challenges in creating a co-registered 3D speckle surface plot is the low resolution of the NanEye cameras. This challenge must be overcome for both the 3D surface plots as well as the LSCI. To create 3D surface plots, the probe needs to be deployed well within the working distance of the cameras. This working distance is between 5.0mm and 35.0mm for the optimal resolution. By operating within the working distance, the images acquired will maintain the best resolution. The better the resolution it is more probable that there will be a higher number of matched features. The greater the number of matched features means there is less extrapolation needed to generate a surface map of the ROI. At these distances, sufficient features can be matched to accurately plot a 3D surface of the ROI.

Ultimately, a prototype endoscope probe was created that had the functionality to perform 3D measurements as well as provide relative flow information. This probe was 7.0mm in diameter and 20.0mm in length. A co-registered laser speckle 3D surface map was generated using the same tube from the flow experiments where a pair of stereo images was taken before the flow data was collected. As before, the tube was probe was placed 15.0mm above the tube and 25 spatially processed contrast images were averaged together to generate the laser speckle contrast image. A ROI of 2.0 mm by 1.75mm was selected to generate matched features over the tube and the phantom. The resulting 7 matches, occurring both on the tube and on the phantom were used to extrapolate a 3D surface for the rest of the ROI. Finally, the laser speckle contrast image was overlaid on top of the surface plot to generate the combined image seen in Figure 3.1

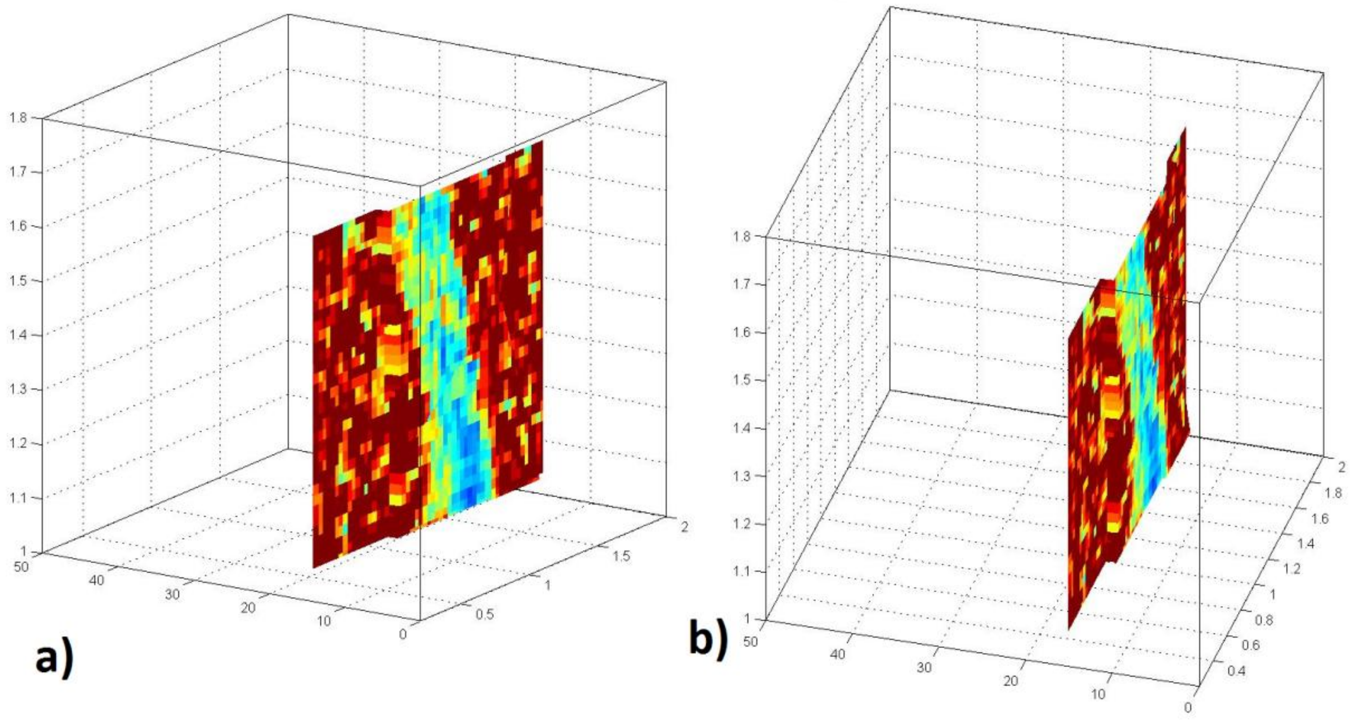

Figure 3.1: Final co-registered 3D laser speckle image. An ROI of the flow phantom was reconstructed as a surface plot and had the same ROI from the speckle contrast image overlaid on top of it

From Figure 3.1, the ROI includes both the tube and the phantom. Half of the tube is elevated 0.5mm above the rest of the phantom. When the distance between the tube and the phantom was computed it yielded a value of .48mm which results in an error of 2.0%. The computed dimensions of the ROI were 1.93mm by 1.62mm, which is an error of 3.5% and 7.4% respectively for the x-y axis. The depth measurement of the tube was computed to be 15.56mm away from the probe with the phantom being 15.01mm away from the probe. Finally, the contrast in the tube averages out to have a contrast of 0.101 which falls in line with previous results at the same flow speed. Figure 3.1 displays a region of the flow phantom that has been accurately mapped to a speckle contrast image. The calculated dimensions of the surface map have similar accuracy to other 3D endoscopic probes such as ones with a structured light approach. To compute the entire co-registered 3D speckle image took 4.56 sec of processing power after all data was acquired. This time could fluctuate depending on the size of the ROI, number of features matched, and number of extrapolated points needed to generate the full surface map. Additionally, depending on the number of matched features, the overall error of the surface plot may vary as well. Regions that have little to no matched features may be incorrectly assigned coordinates that are not exact. This can be overcome by localizing ROIs over areas with many distinct features. To summarize the results given in Figure 3.1, the co-registered 3D speckle endoscopic probe yielded comparable results to other 3D endoscopic technologies with minimal error.

Chapter 5: Conclusion and Summary

As previously mentioned, the goal of this work was to create a new endoscopic probe that would combine 3D measurements with flow analysis into one co-registered quantitative format. In order to achieve this there were two functionalities that had to be validated; the 3D triangulation and the laser speckle contrast imaging.

First, the 3D triangulation was validated. Here the combined usage of stereo viewing and feature matching was implemented to triangulate matched features in terms of real space coordinates. By establishing the resolution of the NanEye cameras it was possible to gauge the level of accuracy when triangulating features. It was determined that the NanEye cameras had a resolution of 140μm while operating in the specified working range of the cameras. This was later validated by the 3D triangulated study where depth (Z-axis) and length (XY-axis) were computed and compared against the measured depths and lengths of known objects. The triangulation results confirmed the expected accuracy based upon the resolution test described in Chapter 2. Comparing these results to existing 3D endoscopic imaging modalities demonstrates that the pairing of stereoscopic imaging yielded comparable measurements.

Next, the NanEye cameras were validated to determine if they possessed sensitivity comparable to that of a lab grade device, by measuring laser speckle contrast values. In order to accomplish this, the NanEye was compared to a Point Grey Chameleon in two experiments; an *ex-vivo* flow experiment and an *in-vivo* occlusion study. Starting with an *ex-vivo* flow study it was determined that the relative flow rates measured by the NanEye resulted in no statistically significant difference to flow rates that were determined by the Chameleon camera. Furthermore, the *in-vivo* occlusion study found that both the NanEye and the Chameleon yielded similar sensitivity measurements for a given patient. By performing both an *ex-vivo* and an *in-vivo* study it was shown that the NanEye does possess the sensitivity to measure flow changes on a physiological level. After both validation studies were conducted, the co-registered 3D speckle endoscope was confirmed to provide 3D reconstructed surfaces measurements on the order of 100μm. The prototype endoscope also displayed a similar sensitivity, an average of 8.8% difference, compared to the results from the Chameleon. These results are comparable with the with previously established technologies such as 3D endoscopes using dual aperture or structured light or other lab-grade LSCI cameras. In the end, combining these two functionalities yielded a new prototype that increases the information gained during minimally invasive procedures. This prototype provides for both a 3D perspective as well as accurate flow information during endoscopic procedures. By creating a fast and effective method of measuring objects or flow inside the body a new method for tracking a patient's condition can now be implemented.

5.1 Limitations

The accuracy of this prototype is still based on feature matching, which can lead to triangulation errors as discussed previously. The triangulated coordinates will remain accurate so long as the coordinates from the matched features are precise. This limitation means that an object requires definable spatial features that can be matched by SIFT and

SURF. Without precise feature matching the triangulated 3D coordinates will not yield accurate results.

The probe is also limited by the working distance of the NanEye cameras. Due to the narrow working distance operational window, any distance exceeding 35mm will cause a decrease in resolution. This will then result in an increase in false matches between the image pair resulting in incorrect triangulated coordinates.

The dynamic range of the NanEye, 0.121, is substantially lower than that of the Chameleon, 0.310. The NanEye allows for less discrete differentiation between contrasts at different flow rates. This is a result of the optical design of the NanEye device.

Finally, the NanEye cameras must be operated with proprietary capture software. This software has significant errors during the capturing of data including frame rate inconsistency, corrupted video formats, and non-uniform timing between two devices. These problems were overcome by employing an older version of the NanEye software and by addressing a variety of minor, yet time consuming technical difficulties. A more streamlined and user accessible version of the software would greatly improve the quality as well as the data acquisition time for future use.

5.2 Future work

While this work provides an important step forward in creating a viable new endoscopic device, there are still some areas to improve upon. Currently, two different sources are used for illumination, one to capture the stereo image pair, and another to capture laser speckle data. One way to streamline the process would be to have a single

PCB board with two distinct sources that can be automatically toggled through a user interface. This would replace the need to manually change the fiber from one source to the other when collecting data.

There is an existing need for the inclusion of additional imaging or surgical functionalities. Incorporating a working channel into the device would create sufficient space for the addition of tools for biopsies or tissue ablation. These are standard tools that are used in endoscopic procedures and thus could benefit from greater efficacy when combined with the co-registered 3D laser speckle surface image. Surgeons could more accurately biopsy or excise polyps and lesions with a better understanding of the blood flow surrounding the area of interest.

Finally, additional cameras could be placed with different overlapping vantage points to create surround 3D imaging. The high field of view of the NanEye would enable multiple vantage points to be stitched together to create a surround image view, while using a minimal number of sensors. The increased visual scene could allow surgeons to view regions that would require extra time to examine thereby reducing procedure time. If even only a few of these challenges were overcome it has the potential to alter the way surgeons track, diagnose, and evaluate patients in the future.

References

---

[1] Picano, Eugenio. "Sustainability of medical imaging: doctors and patients should be more aware of the long term risks of radiological investigations." *British Medical Journal* 328.7439 (2004): 578-581.

[2] Gibson, A. P., J. C. Hebden, and Simon R. Arridge. "Recent advances in diffuse optical imaging." *Physics in medicine and biology* 50.4 (2005): R1.

[3] Boas, David A., Anders M. Dale, and Maria Angela Franceschini. "Diffuse optical imaging of brain activation: approaches to optimizing image sensitivity, resolution, and accuracy." *Neuroimage* 23 (2004): S275-S288.

[4] Boas, D. A., et al. "Improving the diffuse optical imaging spatial resolution of the cerebral hemodynamic response to brain activation in humans." *Optics letters* 29.13 (2004): 1506-1508.

[5] Pogue, Brian W., et al. "Quantitative Hemoglobin Tomography with Diffuse Near-Infrared Spectroscopy: Pilot Results in the Breast 1." *Radiology* 218.1 (2001): 261-266.

[6] Boas, David A., et al. "Noninvasive imaging of cerebral activation with diffuse optical tomography." *In vivo optical imaging of brain function* 39 (2002).

[7] Fan, Yichen, and Max Q-H. Meng. "3D reconstruction of the WCE images by affine SIFT method." *Intelligent Control and Automation (WCICA), 2011 9th World Congress on*. IEEE, 2011.

[8] Ayata, Cenk, et al. "Laser speckle flowmetry for the study of cerebrovascular physiology in normal and ischemic mouse cortex." *Journal of Cerebral Blood Flow & Metabolism* 24.7 (2004): 744-755.

[9] Hecht, Nils, et al. "Intraoperative monitoring of cerebral blood flow by laser speckle contrast analysis." *Neurosurgical focus* 27.4 (2009): E11.

[10] Rajan, Vinayakrishnan, et al. "Influence of tissue optical properties on laser Doppler perfusion imaging, accounting for photon penetration depth and the laser speckle phenomenon." *Journal of biomedical optics* 13.2 (2008): 024001-024001.

---

[11] Sadeg M. Faris; Novel 3D stereoscopic imaging technology. Proc. SPIE 2177, Stereoscopic Displays and Virtual Reality Systems, 180 (April 15, 1994); doi:10.1117/12.173875.

[12] Pankaj, Dhanya S., Rama Rao Nidamanuri, and P. Bhanu Prasad. "3-D Imaging Techniques and Review of Products." *Proceedings of International Conference on" Innovations in Computer Science and Engineering*. 2013.

[13] Westheimer, Gerald. "Three-dimensional displays and stereo vision." *Proceedings of the Royal Society of London B: Biological Sciences* (2011): rspb20102777.

[14] Thirion, J-P. "Image matching as a diffusion process: an analogy with Maxwell's demons." *Medical image analysis* 2.3 (1998): 243-260.

[15] Lowe, David G. "Distinctive image features from scale-invariant keypoints." *International journal of computer vision* 60.2 (2004): 91-110.

[16] Bay, Herbert, et al. "Speeded-up robust features (SURF)." *Computer vision and image understanding* 110.3 (2008): 346-359.

[17] Bae, Sam Y., et al. "Development of a miniature single lens dual-aperture stereo imaging system towards stereo endoscopic imaging application." *Optical Engineering* 51.10 (2012): 103202-1.

[18] Li, Jianan, et al. "High speed miniature motorized endoscopic probe for optical frequency domain imaging." *Optics express* 20.22 (2012): 24132-24138.

[19] Schmalz, Christoph, et al. "An endoscopic 3D scanner based on structured light." *Medical Image Analysis* 16.5 (2012): 1063-1072.

[20] Tippetts, Beau, et al. "Review of stereo vision algorithms and their suitability for resource-limited systems." *Journal of Real-Time Image Processing* 11.1 (2016): 5-25.

[21] Chan, Heang-Ping, et al. "ROC study of the effect of stereoscopic imaging on assessment of breast lesions." *Medical physics* 32.4 (2005): 1001-1009.

---

[22] Westwood, J. D. "In-vivo stereoscopic imaging system with 5 degrees-of-freedom for minimal access surgery." *Medicine Meets Virtual Reality 12: Building a Better You: the Next Tools for Medical Education, Diagnosis, and Care* 98 (2004): 234.

[23] Wieringa, F. P., et al. "Remote non-invasive stereoscopic imaging of blood vessels: First in-vivo results of a new multispectral contrast enhancement technology." *Annals of biomedical engineering* 34.12 (2006): 1870-1878.

[24] Lazaros, Nalpantidis, Georgios Christou Sirakoulis, and Antonios Gasteratos. "Review of stereo vision algorithms: from software to hardware." *International Journal of Optomechatronics* 2.4 (2008): 435-462.

[25] Chan, Manhong, et al. "Miniaturized three-dimensional endoscopic imaging system based on active stereovision." *Applied optics* 42.10 (2003): 1888-1898.

[26] Wu, Qing, and Yizhou Yu. "Feature matching and deformation for texture synthesis." *ACM Transactions on Graphics (TOG)* 23.3 (2004): 364-367.

[27] Lowe, David G. "Object recognition from local scale-invariant features." *Computer vision, 1999. The proceedings of the seventh IEEE international conference on*. Vol. 2. Ieee, 1999.

[28] Panchal, P. M., S. R. Panchal, and S. K. Shah. "A comparison of SIFT and SURF." *International Journal of Innovative Research in Computer and Communication Engineering* 1.2 (2013): 323-327.

[29] Su, Xianyu, and Qican Zhang. "Dynamic 3-D shape measurement method: a review." *Optics and Lasers in Engineering* 48.2 (2010): 191-204.

[30] Hartley, Richard I., and Peter Sturm. "Triangulation." *Computer vision and image understanding* 68.2 (1997): 146-157.

[31] Briers, J. David, and Sian Webster. "Laser speckle contrast analysis (LASCA): a nonscanning, full-field technique for monitoring capillary blood flow." *Journal of biomedical optics* 1.2 (1996): 174-179.

[32] Boas, David A., and Andrew K. Dunn. "Laser speckle contrast imaging in biomedical optics." *Journal of biomedical optics* 15.1 (2010): 011109-011109.

---

[33] Kirkpatrick, Sean J., Donald D. Duncan, and Elaine M. Wells-Gray. "Detrimental effects of speckle-pixel size matching in laser speckle contrast imaging." *Optics letters* 33.24 (2008): 2886-2888.

[34] Huang, Yu-Chih, et al. "Noninvasive blood flow imaging for real-time feedback during laser therapy of port wine stain birthmarks." *Lasers in surgery and medicine* 40.3 (2008): 167-173.

[35] Cheng, Haiying, and Timothy Q. Duong. "Simplified laser-speckle-imaging analysis method and its application to retinal blood flow imaging." *Optics letters* 32.15 (2007): 2188-2190.

[36] Richards, Lisa M., et al. "Low-cost laser speckle contrast imaging of blood flow using a webcam." *Biomedical optics express* 4.10 (2013): 2269-2283.

[37] Ramirez-San-Juan, Julio C., et al. "Spatial versus temporal laser speckle contrast analyses in the presence of static optical scatterers." *Journal of biomedical optics* 19.10 (2014): 106009-106009.

[38] Yang, Owen, and Bernard Choi. "Laser speckle imaging using a consumer-grade color camera." *Optics letters* 37.19 (2012): 3957-3959.

[39] Yuan, Shuai, et al. "Determination of optimal exposure time for imaging of blood flow changes with laser speckle contrast imaging." *Applied optics* 44.10 (2005): 1823-1830.